



HAL
open science

Probing non-Hermitian zero modes in a nanophotonic trimer: From nonuniform to twisted coupling

Melissa Hedir, Kaiwen Ji, Juan Ariel Levenson, Ramy El-Ganainy, Li Ge, Alejandro Yacomotti

► **To cite this version:**

Melissa Hedir, Kaiwen Ji, Juan Ariel Levenson, Ramy El-Ganainy, Li Ge, et al.. Probing non-Hermitian zero modes in a nanophotonic trimer: From nonuniform to twisted coupling. *Physical Review A*, 2024, 110 (4), pp.043515. 10.1103/PhysRevA.110.043515 . hal-04798889

HAL Id: hal-04798889

<https://hal.science/hal-04798889v1>

Submitted on 22 Nov 2024

HAL is a multi-disciplinary open access archive for the deposit and dissemination of scientific research documents, whether they are published or not. The documents may come from teaching and research institutions in France or abroad, or from public or private research centers.

L'archive ouverte pluridisciplinaire **HAL**, est destinée au dépôt et à la diffusion de documents scientifiques de niveau recherche, publiés ou non, émanant des établissements d'enseignement et de recherche français ou étrangers, des laboratoires publics ou privés.

Probing non-Hermitian zero modes in a nanophotonic trimer: from non-uniform to twisted coupling

Melissa Hedir, Kaiwen Ji, and Juan Ariel Levenson

*Centre de Nanosciences et de Nanotechnologies, CNRS, Université Paris-Sud,
Université Paris-Saclay, 10 Boulevard Thomas Gobert, 91120 Palaiseau, France*

Ramy El-Ganainy

Department of Physics, Michigan Technological University, Houghton, Michigan 49931, USA

Li Ge

*Department of Engineering Science and Physics,
College of Staten Island, CUNY, Staten Island, NY 10314, USA and
The Graduate Center, CUNY, New York, NY 10016, USA*

Alejandro M. Yacomotti

*Centre de Nanosciences et de Nanotechnologies, CNRS, Université Paris-Sud,
Université Paris-Saclay, 10 Boulevard Thomas Gobert, 91120 Palaiseau, France and
Laboratoire Photonique Numérique et Nanosciences, Institut d’Optique d’Aquitaine,
Université Bordeaux, CNRS, 33405 Talence, France**

Topological lasers based on optical cavity arrays –such as the Su-Schrierfer-Heeger (SSH) array– in active media have been recently realized in various platforms. In all these studies the coupling coefficient between any adjacent sites of the lattice was positive. Consequently, the lasing mode featured an out of phase oscillation which is typically impractical for any application because it weakens the far field intensity. This problem can be mitigated by altering the coupling signs along the array. However, implementing negative evanescent coupling in microrings, microdisks or micropillars is not possible using standard designs and fabrication processes. In this work, we design and experimentally implement a photonic crystal cavity array that consists of three sites where the sign of one coupling parameter is inverted, which enables the observation of an in-phase topological zero mode. The photonic crystal array presented here utilizes the recently proposed “image barrier” technique, where the photonic barriers are copied at opposite sides of the array, which mitigates chain-termination effects, and at the same time enables sign flip from one barrier to the adjacent one, resulting in “twisted coupling”. Consequently the overall symmetry of the zero mode is inverted and becomes even, which is experimentally demonstrated. Our work opens the door for implementing a new generation of phase-locked topological laser arrays that oscillates in the same phase with enhanced far field optical intensities.

I. INTRODUCTION

Topological zero modes in optics and photonics are collective excitations of coupled waveguide or cavity arrays whose frequency is pinned to a particular point of the optical spectrum [1]. These states have attracted considerable attention recently due to their robustness against a certain class of perturbation. The topological features of these modes are *warranted* by one or more underlying lattice symmetries such as chiral (also known as sublattice) symmetry [2–11] and particle-hole symmetry [12–14]. For instance, in one dimensional geometries such as the Su-Schrierfer-Heeger (SSH) array, these modes arise because of chiral symmetry. As a result, the eigenfrequencies associated with these modes are robust against variation in the nearest neighbour coupling distribution. In non-Hermitian systems featuring optical gain and loss, however, chiral symmetry does not pin a zero mode un-

less the latter is also guaranteed by the Lieb theorem. An even number of non-zero modes might become degenerate at the zero mode energy as a function of a system parameter, but they emerge again as non-zero modes when this parameter is further tuned.

Nevertheless, there are also zero modes in non-Hermitian systems that are *protected* by a given symmetry, which allows them to survive within a sizeable neighborhood in parameter space, such as gain/loss perturbation in the cavities. For example, in the case of non-Hermitian particle-hole symmetry (NHPH), the energy eigenvalues come in pairs satisfying $\Omega_i = -\Omega_j^*$, where Ω is the complex eigenfrequency. As a result, the non-Hermitian zero modes evolves along the imaginary axis of the complex plane [$\Re(\Omega_i) = 0$] for a whole range of spatial perturbation of the pump beams [13, 14]. Because of this symmetry protection, photonic zero modes become compatible with a high degree of freedom in the coupling design, which makes them interesting for applications in topological lasers [15–18] and laser mode engineering [13, 19], as well as in the context of a recent

* alejandro.giacomotti@institutoptique.fr

proposal for applications in optical computing [20].

Small non-Hermitian cavity arrays, such as a linear SSH array of three evanescently coupled cavities (a “photonic trimer”), are minimal systems exhibiting zero modes. Recently, zero modes in coupled photonic crystal (PhC) nanocavities have been demonstrated through spatially-resolved micro photoluminescence experiments [21]. Such zero modes arise from the Lieb’s theorem in the effective Hermitian limit (i.e., with uniform gain or loss across the array), which guarantees their existence provided that the number of cavities is odd. They persist in the presence of non-uniform gain and loss, thanks to the protection from the NHPH symmetry. In Ref. [21], only one pump spot has been utilized, which was not efficient enough to bring the non-Hermitian zero mode above the laser threshold. This is because the zero mode was close to the dark mode of the Hermitian counterpart array, *i.e.* it was mostly localized in the extreme cavities with only a few percent of intensity in the center one, hence difficult to excite with a single light spot. In a subsequent work, such a “dark-like” zero mode was brought above the laser threshold through the spatial patterning of the pump beam using a spatial light modulator (SLM) [22]. In this latter study, the laser zero mode could be observed as the excitation was maximum in the two extreme cavities, and it has been shown to be robust against a certain amount of pump-unbalance. Importantly, these lasing zero modes inherit much of their Hermitian counterpart (i.e. the zero modes of the passive cavity array without gain or loss). In particular, they feature: i) dark-mode characteristics, where the intensity of the center cavity vanishes; ii) anti-symmetric field distribution, arising from π phase jump between the extreme cavities. The first of these features is a direct consequence of chiral symmetry while the second arises because of the positive coupling coefficients between the neighboring elements. As a result, coupling these lasing modes to the outside world is challenging. In addition, in these previous studies, coupling perturbation effects have not been investigated.

In this work, we consider zero-modes in PhC arrays of a different regime. Namely, we investigate a three-coupled cavity array with two different couplings, that can be seen as the embryo of a larger SSH chain. While PhC topologically protected modes have already been reported in PhC coupled cavity arrays [23], here we propose a twisted coupling configuration to induce in-phase oscillation, focusing on a minimal coupled cavity array. In order to realize such symmetry-protected zero modes, all the PhC cavities must have the same resonance frequency. However, the unavoidable edge effects causes

the outer cavities to have slight detuning from the inner ones. To mitigate this problem, we employ what we call an “image barrier” design, which consists in copying photonic barriers at opposite sides of the nanocavities. This technique, together with the barrier engineering approach, provides enough degrees of freedom for controlling the coupling sign between any two adjacent cavities. By taking advantage of this feature, we demonstrate a bright zero mode in a PhC cavity array that consists of a nanophotonic trimer with alternating coupling sign, thus resulting in an in-phase zero mode. It is important to note that while negative coupling can be achieved in laser written waveguides [24], these platforms are not suitable for laser applications due to the difficulty of including gain medium and controlling the pump profile. In addition, the technique proposed in [24] relies on introducing extra elements (waveguides) with precise detuning which increases the complexity of the system. On the other hand, the photonic crystal platform used here is planar which offers two advantages: (1) It is compatible with laser systems as has been demonstrated by numerous groups including ours (our experiment here is implemented using III-V semiconductor material platform as we discuss later in detail), and (2) It can be pumped optically from the top which allows for controlling pumping profiles to study different lasing regimes. Additionally, the planar nature of our geometry makes it ideal for implementing other exotic topological structures that required 2D optical lattices [25–28]. Equally interestingly, our platform can in principle allow for extending these previous studies to the lasing regimes and investigating the interplay between their topological features and non-linear laser dynamics. Our work then provides the proof-of-concept towards the realization of in-phase topological modes in one dimensional active photonic arrays, which could prove useful for building a next generation of topological laser systems.

II. ZERO MODES IN A PHOTONIC TRIMER: MODEL PREDICTIONS

We consider the system depicted in Fig. 1, which consists in three evanescently coupled optical cavities ($n = 1, 2, 3$) with linear resonant frequencies $\omega_{0,n}$ together with cavity damping times τ_n that we assume all identical ($\omega_{0,n} = \omega_0$, $\tau_n = \tau$), and conservative coupling parameters K_{12} and K_{23} , which are different in general. Within a coupled mode theory, the equations of motion read:

$$\frac{da}{dt} = -iHa,$$

$$H = \begin{pmatrix} \omega_0 + \alpha_H g_1 + \Delta\omega_1 & K_{12} & 0 \\ K_{12} & \omega_0 + \alpha_H g_2 + \Delta\omega_2 & K_{23} \\ 0 & K_{23} & \omega_0 + \alpha_H g_3 + \Delta\omega_3 \end{pmatrix} + i \begin{pmatrix} g_1 - \frac{1}{\tau} & 0 & 0 \\ 0 & g_2 - \frac{1}{\tau} & 0 \\ 0 & 0 & g_3 - \frac{1}{\tau} \end{pmatrix}, \quad (1)$$

where $g_n = -\alpha(\mathcal{N}_n)\Gamma/2cn_r$ are the gain coefficients, Γ is the filling factor of the gain medium, c the speed of light, n_r the effective refractive index of the transparent medium, \mathcal{N} the charge-carrier density in cavity n and $\alpha(\mathcal{N})$ the carrier-dependent absorption of the active material. Here we use a logarithmic model for the saturable absorption suitable for semiconductor quantum wells (QWs) where \mathcal{N} varies over a wide range of values (from well below transparency to carrier saturation)[21]:

$$\alpha(\mathcal{N}) = -\frac{\omega_0}{cn_r} \cdot \log\left(\frac{\mathcal{N} + A}{\mathcal{N}_0 + A}\right), \quad (2)$$

where A is a constant and \mathcal{N}_0 the carrier density at QW transparency. The terms $\alpha_H g_n$ in Eq. 1, where α_H is the Henry factor of the QWs, account for carrier-dependent refractive index change and lead to pump induced resonance blue-shift. The passive —cold cavity— detunings are $\Delta\omega_n$. Note that the real matrix in Eq. 1 accounts for the energy conserving —Hermitian— Hamiltonian, while the imaginary part is the non-Hermitian operator.

We first discuss non-Hermitian zero modes in the simplest case where $\alpha_H = 0$, i.e. in the absence of any pump-induced blue-shift effect, and where the passive detunings are equal ($\Delta\omega_n = \Delta\omega$), which will be possible in the actual PhC cavity system by means of the image barrier technique discussed in the next Section; we choose the origin of frequency to be $\omega_0 + \Delta\omega$, i.e. $\omega \rightarrow \omega - (\omega_0 + \Delta\omega)$, such that zero modes verify $\omega = 0$. Let us assume that the cavity 3 is pumped with $\mathcal{N}_3 = 0.23$ ($g_3 = 1.045\tau^{-1}$), and we let the gain in cavity 1 vary from $\mathcal{N}_1 = 0$ [$g_1 = -3.57\tau^{-1}$, black squares in Fig. 1(a)] to $\mathcal{N}_1 = \mathcal{N}_3$ [black crosses in Fig. 1(a)]. The trajectories of the eigenvalues are displayed in Fig. 1(a) for $K_{12} = 15.02\tau^{-1}$ and $K_{23} = 12.36\tau^{-1}$, showing the evolution of the complex eigenvalues ε as the pump is increased in the left cavity; note that the imaginary part of the zero mode frequency gets close to zero at the final state, therefore lasing oscillation is predicted for such a mode. This has been experimentally demonstrated in Ref [22] for equal couplings.

It can be observed in Figs. 1(b)-(c) that the non-Hermitian zero mode features $\pi/2$ phase-shift between adjacent cavities (see horizontal bars). Importantly, unlike the uniform coupling case, the zero mode intensity is unbalanced, being largest in the cavity next to the weakest coupling, here the rightmost cavity [green lines in Fig.

1(b)-(c)] which is close to K_{23} . Note that, in the general case where the pumping is different in the two extreme cavities [as in Fig. 1(b)] the central cavity intensity is nonzero. However, as the two pump intensities become equal [Fig. 1(c)] the central cavity intensity of the zero mode vanishes. The latter case reduces to a dark zero mode and geometric frustration, analogous to the purely Hermitian case. The intensity imbalance can be easily explained in the dark zero mode case of Fig. 1(c) by setting $a_n = A_n \exp(-i\varepsilon t)$ and $A_2 = 0$ in Eq. 1, leading to

$$\frac{A_3}{A_1} = -\frac{K_{12}}{K_{23}}. \quad (3)$$

We stress that Eq. 3 no longer holds in the general case of non-uniform pumping, for instance of Fig. 1(b), because the central cavity intensity becomes nonzero. However, since the latter is only a few percent of the total mode energy, Eq. 3 remains approximately valid, which can be justified using a perturbation theory (see, for example, Ref. [29]). As a result, the mode energy distribution generally follows the rule of larger intensity in the cavity next to the weakest coupling, which holds even when the weakest intensity —in the example Fig. 1, the leftmost— cavity is pumped at a higher level compared to the cavity with the highest intensity —in the example Fig. 1, the rightmost— one.

It is important to point out that the zero mode oscillates out-of-phase as long as the two coupling signs are the same [Figs. 1(b)-(c)]. When only one coupling sign is flipped, the overall symmetry gets inverted as revealed in Figs. 1(d)-(e), for $K_{12} = -24.92\tau^{-1}$. We will show in the following section that such a zero mode, when imaged in the far field, features a local maximum at the normal direction of emission, consistent with the overall symmetric field distribution. From the applications viewpoint, zero-modes with “twisted coupling” are potentially interesting for improving photon collection.

Including the pump-induced blue-shift effects, modeled here through the α_H -factor in Eq. 1, has the consequence of blue shifting all the modes. Red trajectories in Fig. 1(a), obtained for $\alpha_H = 3$, depict the evolution of eigenvalues as the pump intensity in cavity 1 is increased, while that in cavity 3 remains fixed. Note that the two-spot pumping configuration efficiently excites the zero mode laser, even in the presence of blue-shift effects [22]. Importantly, the nonzero α_H -factor also modifies

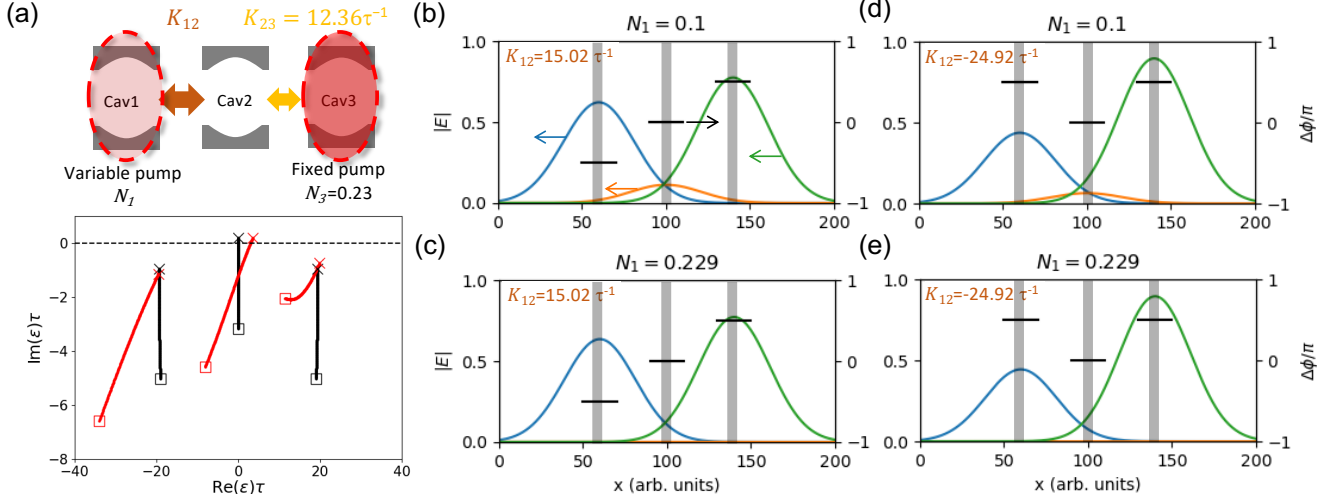


FIG. 1. Zero mode with non-uniform couplings: field localization and non-Hermiticity. (a) Top: schematics of three evanescently coupled cavities with different coupling parameters: $K_{23} = 12.36\tau^{-1}$ is fixed, K_{12} is varied. Bottom: evolution of the mode frequencies as cavity 1 is pumped from $N_1 = 0$ (squares) to $N_1 = 0.23$ (crosses), for $K_{12} = 15.02\tau^{-1}$. Black: $\alpha_H = 0$, and red: $\alpha_H = 3$. Field amplitude and phase spatial distributions from the CMT model with: (b)-(c) $K_{12} = 15.02\tau^{-1}$ (corresponding to a barrier perturbation parameter of $h_{12} = 0.1$, see Sec. III); (d)-(e) twisted coupling with $K_{12} = -24.92\tau^{-1}$ (corresponding to a barrier perturbation parameter of $h_{12} = -0.35$). The photon lifetime is $\tau = 7$ ps. Cavities are located at $x_1 = 60$, $x_2 = 100$ and $x_3 = 140$. The extension of the gaussian pump profile is $\sigma = 40$ (see Appendix), and the colored lines in (b)-(e) represent the cavity intensities $I_n^{(j)}(x)$, modelled as $I_n^{(j)}(x) = |E_n^{(j)}(x)|^2$, where $E_n^{(j)}(x) = \exp[-(x - x_n)^2/\sigma_c^2]A_n^{(j)}$, with $\sigma_c = 30$ and $A_n^{(j)}$ the cavity amplitudes of mode j . Vertical gray bars indicate the cavity positions. $\alpha_H = 0$ in (b)-(e).

the cavity phases, while essentially preserving the phase difference between the two extreme cavities. Such phase perturbations, however, have important consequences in the mode radiation patterns, as will be discussed in Sec. III B.

III. RESULTS

We fabricated suspended Indium Phosphide (InP)-membranes containing three coupled PhC L3 nanocavities with embedded $\text{InGa}_{0.17}\text{As}_{0.76}\text{P}$ QWs, whose photoluminescence (PL) is centered about $\lambda = 1520$ nm. We have designed the central hole-row in the PhC barriers with radius $r_3 = r_0(1 + h)$, r_0 being the hole radius of the underlying PhC lattice ($r_0 = 0.266a$, a is the period of the triangular lattice lying in the range 400 – 420 nm). We call the parameter h ($|h| < 1$) the barrier perturbation. In order to increase the Q-factor [30], the two holes closing each cavity have a reduced radius $r_1 = r_0 - 0.06a$ and are shifted apart by $s = 0.16a$. Also holes around the cavities are modified with a period $2a$ by $r_2 = r_0 + 0.05a$ in order to improve the beaming quality of the emitted light and hence the collection efficiency [31]; consequently, beaming holes inside the barrier have radius $r_4 = r_2(1 + h)$. The coupled cavity structure is displayed in Fig. 2(a), incorporating two different barrier parameters, h_{12} and h_{23} at the left and right sides, respectively.

With the aim of avoiding cavity-to-cavity detuning as a consequence of varying h , we have utilized the image barrier technique that copies opposite barriers at the terminations of the cavity array (details will be published elsewhere). As a result, the three cavity detunings are approximately equal, $\Delta\omega_n \approx \Delta\omega(h_{12}) + \Delta\omega(h_{23})$, where $\Delta\omega(h_{12})$ and $\Delta\omega(h_{23})$ are the cavity detunings in the presence of the modified left and right barrier, respectively.

A. Non-uniform coupling: photoluminescence maps

We have first experimentally characterized the coupling parameter as a function of the barrier perturbation h using a two coupled-cavity configuration. Microphotoluminescence (PL) experiments were performed to measure the emission spectra of the cavities as a function of the spatial position of the illumination spots, which is varied by means of a PZT-driven sample holder. The sample is pumped on the surface using a pulsed (~ 100 ps-pulse duration) laser at $\lambda = 785$ nm through a microscope objective (100x, N.A.=0.95), and the emission is then collected by the same microscope objective and sent to a spectrometer coupled to a nitrogen-cooled infrared sensor. Figure 2(b) shows the coupling parameter as a function of h , which has been obtained from the mode splitting measurements in the photonic dimer.

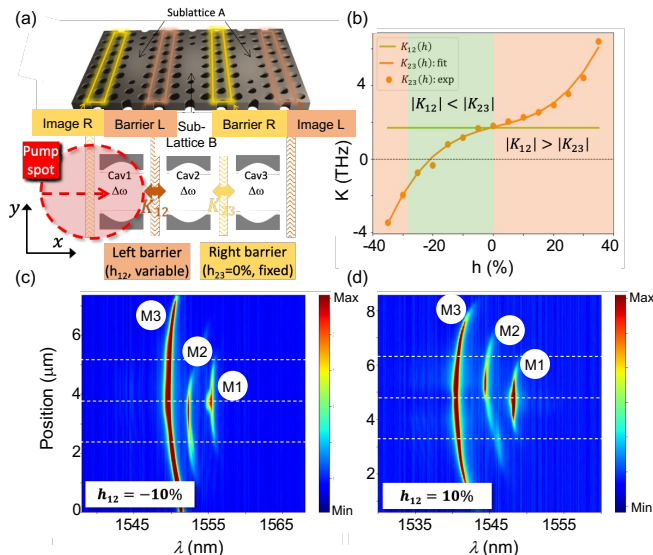


FIG. 2. (a) Schematics of the three coupled PhC L3 nanocavities with image barriers: the left barrier (red) is copied at the right side of cavity 3, and the right barrier (yellow) is copied at the left side of cavity 1, which ensures uniform detuning. (b) Experimental determination of intercavity coupling in a two coupled cavity system as a function of the barrier perturbation. In a three-coupled cavity system where $h_{23} = 0$, the green (red) background stands for regions where $|K_{12}| < |K_{23}|$ ($|K_{12}| > |K_{23}|$). (c)-(d) PL intensity maps upon scanning of a single pump spot across the three coupled cavity system. (c) $h_{12} = -0.1$, where the weakest coupling is the one between cavities 1 and 2, and (d) $h_{12} = 0.1$, where the weakest coupling is the one between cavities 2 and 3. It can be observed that the PL maximum of the central mode (quasi-zero mode) is displaced from the geometrical center (central dashed white line), leaning towards cavity 1 in (c) and towards cavity 3 in (d).

In the three coupled cavity array we fix the right barrier to $h_{23} = 0$ (unperturbed) and fabricate samples with h_{12} ranging from -0.35 to 0.35 . Note that the coupling magnitude between cavities 1 and 2 is weaker than that between cavities 2 and 3 in the range $-0.3 < h_{12} < 0$ [Fig. 2(b), green region], whereas the opposite situation is verified outside this range [Fig. 2(b), orange region]. We then choose two representative cases: $h_{12} = -0.1$ leads to $|K_{12}| < |K_{23}|$ [Fig. 2(c)], and $h_{12} = 0.1$ verifies $|K_{12}| > |K_{23}|$ [Fig. 2(d)]. Later on, we will also investigate the case $h_{12} = -0.35$, featuring coupling sign flip. We collect the PL emission for varying pump spot positions with respect to the cavities. Figures 2(c) and (d) show the PL maps in the two coupling configurations. Three modes can be observed: we call M1 the lowest energy mode which is generally weak, though clearly visible at $\lambda \approx 1555\text{nm}$ in Fig. 2(c), and more intense in Fig. 2(d) at $\lambda \approx 1548\text{nm}$; M3 is the highest-energy mode [at $\lambda \approx 1550\text{nm}$ in Fig. 2(c), and at $\lambda \approx 1540\text{nm}$ in Fig.

2(d)], which is the strongest one; finally, M2 is the zero mode, clearly visible at $\lambda \approx 1553\text{nm}$ and $\lambda \approx 1544\text{nm}$ for $h_{12} = -0.1$ and $h_{12} = 0.1$, respectively. Interestingly, while two symmetric lobes are observed in the case of equal coupling at both sides [21], the case of non-uniform coupling reveals more intense PL when the pump spot is located between the center cavity and one of the two extreme cavities: the bottom one in 2(c), which corresponds to cavity 1, and the top cavity in Fig. 2(d), which corresponds to cavity 3. We attribute this behavior to the intensity imbalance of the zero mode in the presence of non-equal couplings (Eq. 3). Indeed, in the case of Fig. 2(c) the smallest coupling is the bottom one (between cavities 1 and 2), and the situation is reversed in Fig. 2(d) (weakest coupling between cavities 2 and 3). It is important to point out that the PL maps in Figs. 2(c)-(d), although they do not directly quantify the spatial distribution of the mode energy in the cavities, they provide a measure of the spatial overlap of the pump beam with the mode energy distribution. Hence, inverting the location of the weaker photonic barrier also inverts the location of the strongest PL intensity. In Fig. 3(a), the PL intensity map for $h_{12} = -0.1$ is compared with numerical simulations obtained from the carrier-dependent CMT (Eq. A1), for a single pump spot at different locations (X). Despite the simplicity of the model, the experimental results and simulations are in good qualitative—and partially quantitative—agreement. As in a previous work [21], one feature that is well captured by the numerical simulations is the fact that the M2 lobes are not centered at the extreme cavity positions; rather, they are located somewhere at the midway between the center and the extreme cavities.

B. Near and far-field patterns

In order to investigate the spatial energy distribution of the modes, near and far-field patterns are measured for fixed positions of the pump spot using an InGaAs camera. Near field patterns must be understood in the sense of imaging the sample plane on the camera, while far-field patterns are obtained imaging the back-focal plane of the microscope objective [32]. The results for $h_{12} = -0.1$ are shown in Appendix B for nonzero modes, and in Figs. 4(a),(b) for zero modes. Nonzero-mode energy distributions are, overall, in very good agreement with the expectations from CMT calculations. Let us now focus on zero modes [Figs. 4(a),(b)]. Here, in order to excite M2 more efficiently, we use a spatial light modulator (SLM), which allows us to mold the pump spot at will: we use a double spot approximately centered at the extreme cavities. The far-field emission exhibits a node in the center, which is an indication of a π -phase difference between the extreme cavities, also predicted by the CMT model. The coupling imbalance produces some asymmetry in the near-field PL intensity along the x -direction, in the form of a slight intensity localization in the cavity close to the weakest

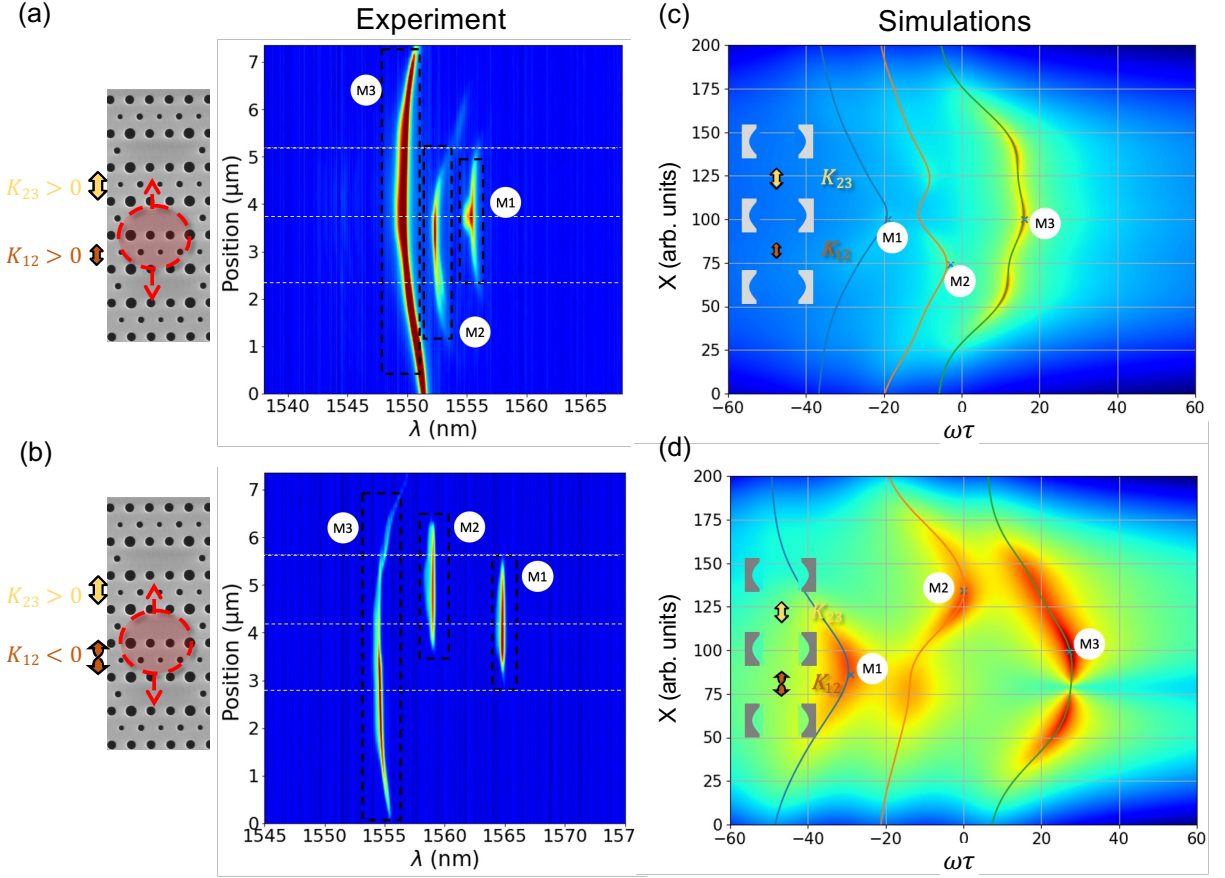


FIG. 3. PL intensity maps upon scanning of a single pump spot. (a),(b) Experimental results. (c),(d) Numerical simulations, $N_{max} = 0.27$. (a) and (c): same coupling sign, $K_{12} = 9.14\tau^{-1}$ ($h_{12} = -0.1$) and $K_{23} = 12.36\tau^{-1}$ ($h_{23} = 0$). (b) and (d): flipped coupling sign, $K_{12} = -24.92\tau^{-1}$ ($h_{12} = -0.35$) and $K_{23} = 12.36\tau^{-1}$ ($h_{23} = 0$). The flipped coupling sign is represented by a twisted red arrow.

coupling, which is expected from Eq. 3. However, at this point, it is important to discuss the presence of pumping-induced blue-shift effects perturbing the relative phase shift of the cavities, as evidenced in the numerical simulations [Fig. 4(b),(c)]. The cavity-to-cavity phase shift of $\pi/2$, typical of a zero mode, is destroyed; instead, for the two pump-spot configuration, about $\sim \pi$ phase shift is predicted between cavities 2 and 3, while there is a small phase difference between cavities 1 and 2. In this respect, the zero modes characterized herein are rather *quasi-zero modes*, while actual zero modes necessitate compensation of the pump-induced detuning, as it has been recently implemented in the nanophotonic dimer in the context of exceptional points [33]. Importantly, the non-Hermitian zero mode is predicted to be a bright mode in general, as evidenced in Fig. 4(c), where the emission is simulated under a single pump-spot excitation. Unlike exciting the zero mode by pumping the two extreme cavities [22], here

the center cavity has nonzero intensity.

Notably, such a carrier-induced phase perturbation has dramatic consequences in the near field patterns. While imaging the sample plane could in principle enable the identification of three distinct lobes accounting for the cavity intensities, this is strongly modified in the presence of carrier-induced blue-shift effects. As it can be observed in Fig. 4(c), the zero mode interference pattern in the near field features two maxima instead of three, due to the constructive interference between cavity fields 2 and 3. In contrast, the intensity of cavity 1 is expected to form an isolated lobe. In the experiment, no more than two maxima are observed regardless of the excitation conditions [one spot –not shown–, and also two spots with different intensities, see Fig. 4(a)], which can then be attributed to such a phase distribution yielding the coherent merging of fields emitted by two adjacent cavities. The predicted numerical phases are confirmed

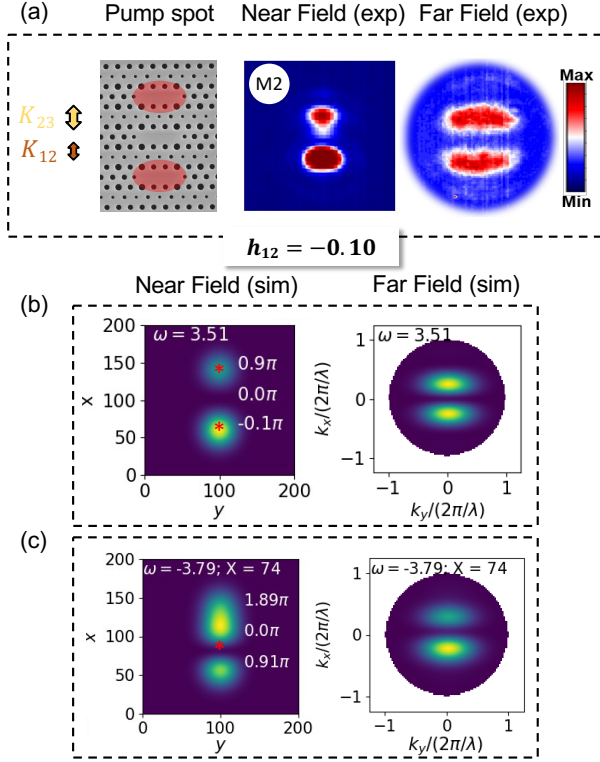


FIG. 4. Spatially resolved mode PL with non-uniform couplings and equal coupling signs: quasi-zero modes. (a) Experimental results, upon two pump-spot illumination. (b),(c) Numerical simulations, under two different pumping profiles. The two coupling parameters are $K_{23} = 12.36\tau^{-1}$ ($h_{23} = 0$) and $K_{12} = 9.14\tau^{-1}$ ($h_{12} = -0.1$). (b) Two excitation points (marked as red asterisks in the near field pattern), $N_1 = 0.229$ and $N_3 = 0.23$, and (c) single excitation point (red asterisk in the near field pattern), corresponding to the X -value at the cross with label M2 in Fig. 3(c). In (b) the zero mode is a dark mode (vanishing intensity in the central cavity), while in (c) it is a quasi zero mode characterized by non-vanishing intensity in the middle cavity.

by the far-field pattern, which always shows a two-lobe-intensity-distribution with a node in the center, which characterizes the overall $\sim \pi$ phase difference between cavities 1 and 3, regardless of the excitation conditions. We conclude that the configuration of two couplings with the same sign is not suitable for assessing the near field pattern of the quasi-zero mode.

C. Zero mode with twisted coupling

We investigated the case of flipped sign of the left barrier (h_{12}), and the results are shown in Fig. 3(b),(d) for the PL map upon pump spot scanning, together with Fig. 5 for the radiation patterns. In this case, the coupling due to the modified barrier $h_{12} = -0.35$ is $K_{12} \approx -3.56$ THz,

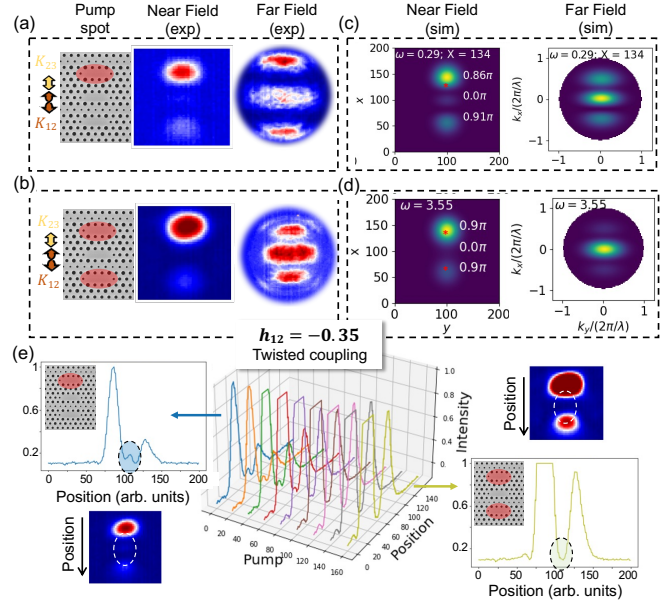


FIG. 5. Spatially resolved PL of the quasi-zero mode with twisted coupling. (a) Single pump spot in cavity 1 [blue curve in (e)]. (b) Twin pump spots in cavities 1 and 3 [yellow curve in (e)]. The intensity in cavity 2 is measurable in (a), and falls below the limit of detection in (b). The coupling sign is flipped between cavities 1 and 2 ($K_{12} = -24.92\tau^{-1}$), represented by a twisted red arrow. (c)-(d) CMT simulations. (e) Intensity cross sections as a function of a pump spot intensity in cavity 3.

is larger in modulus than that of h_{23} ($K_{23} \approx 1.77$ THz), yet the sign is reversed: we call this a *twisted* coupling configuration. Note that the twisted coupling is achieved by choosing a barrier perturbation parameter between cavities 1 and 2 smaller than the degeneracy value, i.e. $h_{12} < -0.2157$.

First, unlike Fig. 4(c), in Figs. 5(a),(c) we observe three distinct lobes corresponding to the emitted photons from each cavity. Second, the far field image of the (quasi) zero mode shows a lobe in the center, and the mode symmetry is overall even [Figs. 5(a)-(d)]. Such a symmetry inversion is the consequence of the twisted coupling, and also drastically modifies the far-field patterns of the other two modes [Figs. 7(b) and (d)]. Let us stress that the near-field image of the zero mode under single pump-spot excitation now exhibits three clear lobes at a pump spot position displaced from the center, *i.e.* upon strongly asymmetric pump. In particular, the center cavity intensity, although weak, is non-vanishing in Fig. 5(a), which demonstrates deviation from the Hermitian dark zero mode, as predicted in Fig. 1(d). Imaging individual emission lobes in the near field of the zero mode can be understood from the numerical simulations of Fig. 5(c), as the phase difference between cavities 1-2 and 2-3 is $\sim 0.9\pi$ in both cases, which induces nodes between adjacent cavity fields.

In a last experiment, we implement our SLM beam shaping starting from the single pump spot in cavity 3, where a weak but nonzero intensity is observed in the center cavity, and turn on a second pump spot in cavity 1 whose intensity is progressively increased [Fig. 5(e) from left to right]. We observe that the center cavity intensity progressively decreases as the pump spot power in cavity 1 is increased, from the single pump spot [Fig. 5(a)] up to the symmetric pumping conditions [Fig. 5(b)], where the intensity in cavity 2 falls below the limit of detection. These results show a behavior compatible with the predictions of Fig. 1: we continuously move from the quasi-zero mode intensity distribution for asymmetric pumping, akin to Fig. 1(d), to the dark-mode of Fig. 1(e) upon symmetric pumping conditions. These results illustrate the ability of a system with twisted coupling to map the PL emission patterns of zero modes to the predicted mode-energy distributions across the cavity array. This is particularly true in the presence of carrier induced refractive index effects, where the resulting near field mode distributions of quasi-zero modes feature nodes between adjacent cavities.

IV. CONCLUSIONS

We have demonstrated bright zero modes in a nanophotonic trimer, formed by three evanescently coupled photonic crystal nanocavities with embedded quantum wells. The nanocavities gain and loss are varied by using a spatial light modulator acting on the pump laser. Bright zero modes have been achieved through the inversion of one coupling parameter's sign, which is enabled by means of the so-called barrier engineering technique. Cavity detuning effects are mitigated by copying photonic barriers on opposite sides of the array, which we denote as "image barriers". Flipping only one coupling sign results in a "twisted coupling" configuration, that proves instrumental for enhancing far-field radiation.

The meaning of bright zero mode must be understood in a twofold sense. First of all, the mode overall symmetry has been inverted, from odd in the otherwise zero mode with equal coupling signs, to even in the case of twisted coupling, which induces a maximum of PL emission in the normal direction of the far-field emission. Second, the center cavity intensity is non vanishing, which is a consequence of the non-Hermitian nature of system under asymmetric pumping. The actual near field radiation pattern could be observed thanks to the twisted coupling geometry that induces field nodes between the

cavities.

In sum, we unveil a coupling geometry to generate in-phase zero modes, which is of paramount importance for applications that exploit their far-field emission. Although the zero-mode investigated here benefits from symmetry instead of topological protection, the system could be easily extended to topologically protected zero modes in SSH chains, similarly to Ref. [34], but using the barrier engineering technique, such that coupling signs can be inverted. It is worth pointing out that non-uniform couplings in topologically protected zero modes not only appear in the alternate form (such as the binary strong and weak couplings in the SSH model and the breathing Kagome lattice) but also in a monotonically varying fashion, as in the recently found selective non-Hermitian skin effect [29]. Furthermore, we believe that the concept of "twisted coupling" provides additional degrees of freedom to engineer laser modes in coupled cavity arrays with embedded gain materials, which might also prove useful for the realization of active corner states by the means of dimerized cavity arrangements [35, 36].

Appendix A: Carrier-dependent coupled mode model

We restrict our theoretical analysis to the spontaneous emission regime —i.e. below laser threshold and neglecting amplification—, in which a linear but carrier-dependent non-Hermitian CMT is valid [21]. We assume in general M -pump spots with gaussian profiles $P(x; X^{(m)}) = \exp[-(x - X^{(m)})^2/\sigma^2]$, centered at given $X^{(m)}$ -positions ($1 \leq m \leq M$), therefore $\mathcal{N}_n = \sum_{m=1}^M \mathcal{N}_{max}^{(m)} P(x_n; X^{(m)})$, where x_n are the central positions of the cavities. The gain in each cavity depends on \mathcal{N} through the QW absorption $\alpha(\mathcal{N})$ (Eq. 2), *i.e.*, $g_n = -\alpha(\mathcal{N}_n)\Gamma/cn_r$ and therefore ε_j depends not only on the pump intensities but also on the pump positions, $\varepsilon_j = \varepsilon_j(\mathbf{X})$, where \mathbf{X} is a vector containing all the pump spot positions $X^{(m)}$. The spontaneous emission in the cavities is $|f\rangle$ ($f_n \propto \mathcal{N}_n$), and the modal excitation amplitudes $f_j(\mathbf{X}) = \langle \Phi_j | f \rangle$, $\langle \Phi_j |$ being the left eigenvectors of \tilde{H} . In this spontaneous emission regime the total emitted spectral intensity can be calculated as the incoherent superposition of the N mode intensities (here $N = 3$), each one contributing with a Lorentzian peak of amplitude $f_j(\mathbf{X})$, resonant frequency $\text{Re}[\varepsilon_j(\mathbf{X})]$ and width $\text{Im}[\varepsilon_j(\mathbf{X})]$ [21]:

$$I(\omega; \mathbf{X}) = \left| \sum_j \frac{f_j(\mathbf{X})}{(\omega - \text{Re}[\varepsilon_j(\mathbf{X})])i + \text{Im}[\varepsilon_j(\mathbf{X})]} \right|^2 \simeq \sum_j \frac{|f_j(\mathbf{X})|^2}{(\omega - \text{Re}[\varepsilon_j(\mathbf{X})])^2 + (\text{Im}[\varepsilon_j(\mathbf{X})])^2}. \quad (\text{A1})$$

Figure 6 shows the calculated spectral intensity maps

$I(\omega; X)$ under spatial scanning of a single Gaussian pump

spot, computed from Eq. A1, for two representative values of coupling imbalance, $h_{23} = 0$ and $h_{12} = \pm 0.1$. The signatures of the zero mode are the two central lobes corresponding to M2. The PL maps show that the intensity is larger in the cavity close to weakest coupling strength. The zero-mode near-field patterns, computed as the coherent superposition of cavity fields, do not allow one to isolate the emissions from cavities 2-3 [Fig. 6(b)] and cavities 1-2 [Fig. 6(d)], because of the constructive interference resulting from a strong blue-shift phase perturbation, as discussed in the main text.

Appendix B: Field radiation patterns of nonzero modes

Figure 7 shows the near and far-field images of nonzero modes in the two different situations: non-uniform cou-

pling but same coupling sign, corresponding to $h_{12} = -0.1$ [Fig. 7 (a,c)], and non-uniform twisted coupling for $h_{12} = -0.35$ [Fig. 6 (b,d)]. There is good agreement between the model predictions and the experimental results overall. Only the far-field of M1 in Fig. 7(a) does not show a clear center lobe as in the numerical calculation; such a discrepancy might be due to a weak emission that falls below the limit of detection of the infrared camera.

-
- [1] T. Ozawa, H. M. Price, A. Amo, N. Goldman, M. Hafezi, L. Lu, M. C. Rechtsman, D. Schuster, J. Simon, O. Zilberberg, and I. Carusotto, *Topological photonics*, *Rev. Mod. Phys.* **91**, 015006 (2019).
- [2] N. Malkova, I. Hromada, X. Wang, G. Bryant, and Z. Chen, Observation of optical shockley-like surface states in photonic superlattices, *Opt. Lett.* **34**, 1633 (2009).
- [3] A. Poddubny, A. Miroschnichenko, A. Slobozhanyuk, and Y. Kivshar, Topological majorana states in zigzag chains of plasmonic nanoparticles, *ACS Photonics* **1**, 101 (2014), <https://doi.org/10.1021/ph4000949>.
- [4] R. El-Ganainy and M. Levy, Optical isolation in topological-edge-state photonic arrays, *Opt. Lett.* **40**, 5275 (2015).
- [5] A. Blanco-Redondo, I. Andonegui, M. J. Collins, G. Harari, Y. Lumer, M. C. Rechtsman, B. J. Eggleton, and M. Segev, Topological optical waveguiding in silicon and the transition between topological and trivial defect states, *Phys. Rev. Lett.* **116**, 163901 (2016).
- [6] Q. Cheng, Y. Pan, Q. Wang, T. Li, and S. Zhu, Topologically protected interface mode in plasmonic waveguide arrays, *Laser & Photonics Reviews* **9**, 392 (2015).
- [7] S. Ke, B. Wang, H. Long, K. Wang, and P. Lu, Topological edge modes in non-hermitian plasmonic waveguide arrays, *Opt. Express* **25**, 11132 (2017).
- [8] F. Bleckmann, Z. Cherpakova, S. Linden, and A. Alberti, Spectral imaging of topological edge states in plasmonic waveguide arrays, *Phys. Rev. B* **96**, 045417 (2017).
- [9] J. Noh, W. A. Benalcazar, S. Huang, M. J. Collins, K. P. Chen, T. L. Hughes, and M. C. Rechtsman, Topological protection of photonic mid-gap defect modes, *Nature Photonics* **12**, 408 (2018).
- [10] L. Lin, S. Kruk, Y. Ke, C. Lee, and Y. Kivshar, Topological states in disordered arrays of dielectric nanoparticles, *Phys. Rev. Res.* **2**, 043233 (2020).
- [11] D. V. Zhirihin and Y. S. Kivshar, Topological photonics on a small scale, *Small Science* **1**, 2170032 (2021).
- [12] M. Pan, H. Zhao, P. Miao, S. Longhi, and L. Feng, Photonic zero mode in a non-hermitian photonic lattice, *Nature Communications* **9**, 1 (2018).
- [13] L. Ge, Symmetry-protected zero-mode laser with a tunable spatial profile, *Physical Review A* **95**, 023812 (2017).
- [14] J. D. H. Rivero and L. Ge, Chiral symmetry in non-Hermitian systems: Product rule and Clifford algebra, *Physical Review B* **103**, 014111 (2021).
- [15] Y. Ota, K. Takata, T. Ozawa, A. Amo, Z. Jia, B. Kante, M. Notomi, Y. Arakawa, and S. Iwamoto, *Nanophotonics* **9**, 547 (2020).
- [16] P. St-Jean, V. Goblot, E. Galopin, A. Lemaitre, T. Ozawa, L. Le Gratiet, I. Sagnes, J. Bloch, and A. Amo, Lasing in topological edge states of a one-dimensional lattice, *Nature Photonics* **11**, 651 (2017), [arXiv:1704.07310](https://arxiv.org/abs/1704.07310) [cond-mat.mes-hall].
- [17] H. Zhao, P. Miao, M. H. Teimourpour, S. Malzard, R. El-Ganainy, H. Schomerus, and L. Feng, Topological hybrid silicon microlasers, *Nature communications* **9**, 981 (2018).
- [18] M. Parto, S. Wittek, H. Hodaie, G. Harari, M. A. Bandres, J. Ren, M. C. Rechtsman, M. Segev, D. N. Christodoulides, and M. Khajavikhan, Edge-mode lasing in 1d topological active arrays, *Phys. Rev. Lett.* **120**, 113901 (2018).
- [19] H. Schomerus, Topologically protected midgap states in complex photonic lattices, *Opt. Lett.* **38**, 1912 (2013).
- [20] G. Tirabassi, K. Ji, C. Masoller, and A. M. Yacomotti, Binary image classification using collective optical modes of an array of nanolasers, *APL Photonics* **7**, 090801 (2022).
- [21] F. Hentinger, M. Hedir, B. Garbin, M. Marconi, L. Ge, F. Raineri, J. A. Levenson, and A. M. Yacomotti, Direct observation of zero modes in a non-hermitian optical nanocavity array, *Photonics Research* **10**, 574 (2022).
- [22] K. Ji, B. Garbin, M. Hedir, J. A. Levenson, and A. Yacomotti, Non-hermitian zero-mode laser in a nanophotonic trimer, *Physical Review A* **107**, L061502 (2023).
- [23] C. Han, M. Lee, S. Callard, C. Seassal, and H. Jeon, Lasing at topological edge states in a photonic crystal L3 nanocavity dimer array, *Light: Science and Applications* **8**, 10.1038/s41377-019-0149-7 (2019).

- [24] R. Keil, C. Poli, M. Heinrich, J. Arkininstall, G. Weihs, H. Schomerus, and A. Szameit, Universal sign control of coupling in tight-binding lattices, *Phys. Rev. Lett.* **116**, 213901 (2016).
- [25] J. Arkininstall, M. Teimourpour, L. Feng, R. El-Ganainy, and H. Schomerus, Topological tight-binding models from nontrivial square roots, *Physical Review B* **95**, 165109 (2017).
- [26] W. A. Benalcazar, B. A. Bernevig, and T. L. Hughes, Quantized electric multipole insulators, *Science* **357**, 61 (2017).
- [27] J. Noh, W. A. Benalcazar, S. Huang, M. J. Collins, K. P. Chen, T. L. Hughes, and M. C. Rechtsman, Topological protection of photonic mid-gap defect modes, *Nature Photonics* **12**, 408 (2018).
- [28] S. Mittal, V. V. Orre, G. Zhu, M. A. Gorlach, A. Poddubny, and M. Hafezi, Photonic quadrupole topological phases, *Nature Photonics* **13**, 692 (2019).
- [29] L. Ge, Non-Hermitian Systems with a Real Spectrum and Selective Skin Effect, *Innov. Discov.* **1**, 4 (2024), see also arxiv:2403.10389.
- [30] Y. Akahane, T. Asano, B.-S. Song, and S. Noda, High- q photonic nanocavity in a two-dimensional photonic crystal, *Nature* **425**, 944 (2003).
- [31] N.-V.-Q. Tran, S. Combrié, and A. De Rossi, Directive emission from high- q photonic crystal cavities through band folding, *Phys. Rev. B* **79**, 041101 (2009).
- [32] S. Haddadi, L. Le-Gratiet, I. Sagnes, F. Raineri, A. Bazin, K. Bencheikh, J. A. Levenson, and A. M. Yacomotti, High quality beaming and efficient free-space coupling in 13 photonic crystal active nanocavities, *Opt. Express* **20**, 18876 (2012).
- [33] K. Ji, Q. Zhong, L. Ge, G. Beaudoin, I. Sagnes, F. Raineri, R. El-Ganainy, and A. M. Yacomotti, Tracking exceptional points above the lasing threshold, *Nature Communications* **14**, 10.1038/s41467-023-43874-z.
- [34] C. Han, M. Lee, S. Callard, C. Seassal, and H. Jeon, Lasing at topological edge states in a photonic crystal 13 nanocavity dimer array, *Light: Science & Applications* **8**, 40 (2019).
- [35] W. A. Benalcazar, B. A. Bernevig, and T. L. Hughes, Quantized electric multipole insulators, *Science* **357**, 61 (2017).
- [36] S. Mittal, V. V. Orre, G. Zhu, M. A. Gorlach, A. Poddubny, and M. Hafezi, Photonic quadrupole topological phases, *Nature Photonics* **13**, 692 (2019).

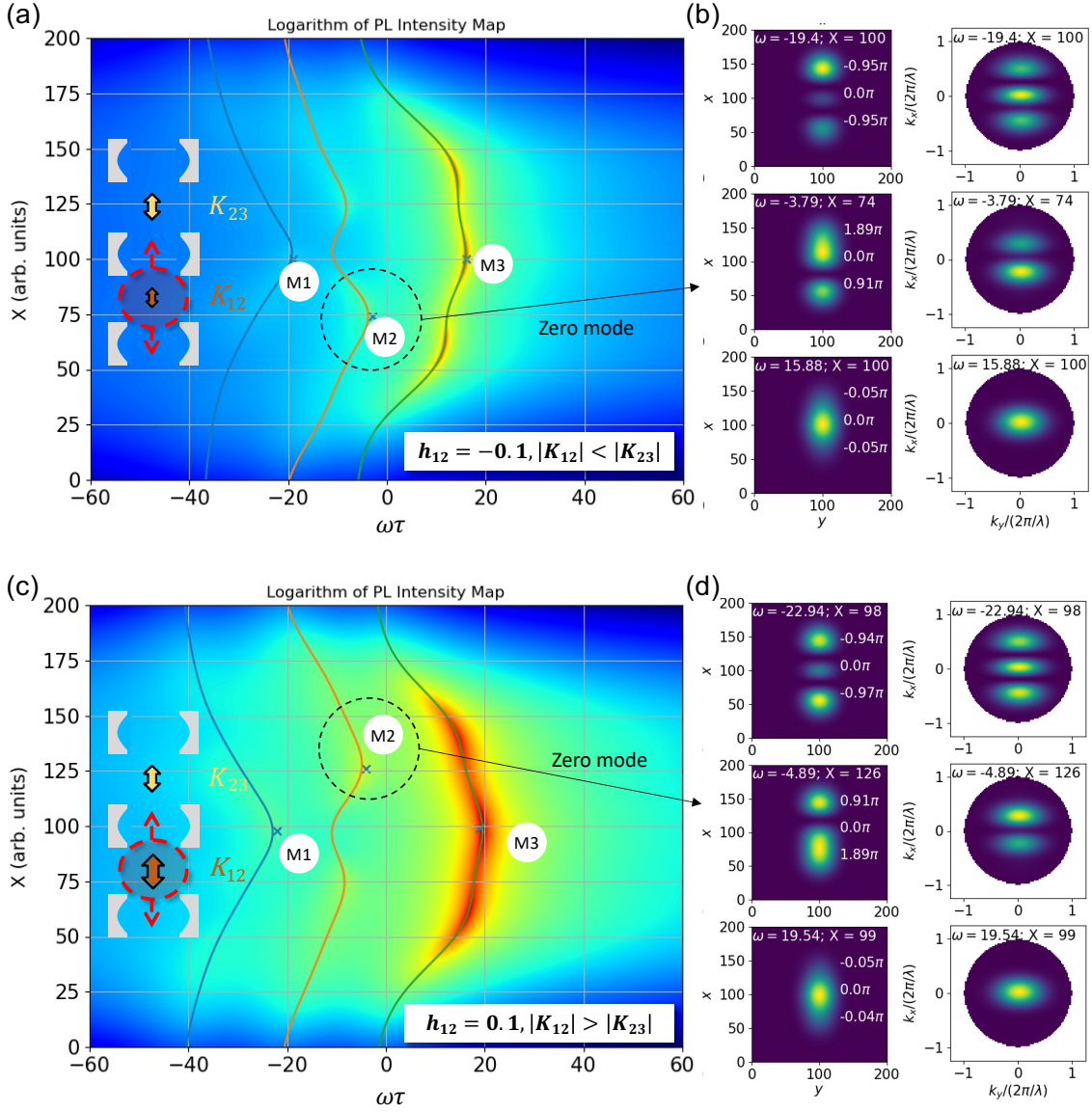


FIG. 6. PL intensity maps and radiation patterns upon scanning of a single pump spot : numerical simulations for equal coupling sign. (a) and (c) Intensity maps. (b) and (d): near (left column) and far (right column) field patterns. $N_{max} = 0.27$ and $K_{23} = 12.36\tau^{-1}$ ($h_{23} = 0$). (a) and (b): $K_{12} = 9.14\tau^{-1}$ ($h_{12} = -0.1$). (c) and (d): $K_{12} = 15.02\tau^{-1}$ ($h_{12} = 0.1$).

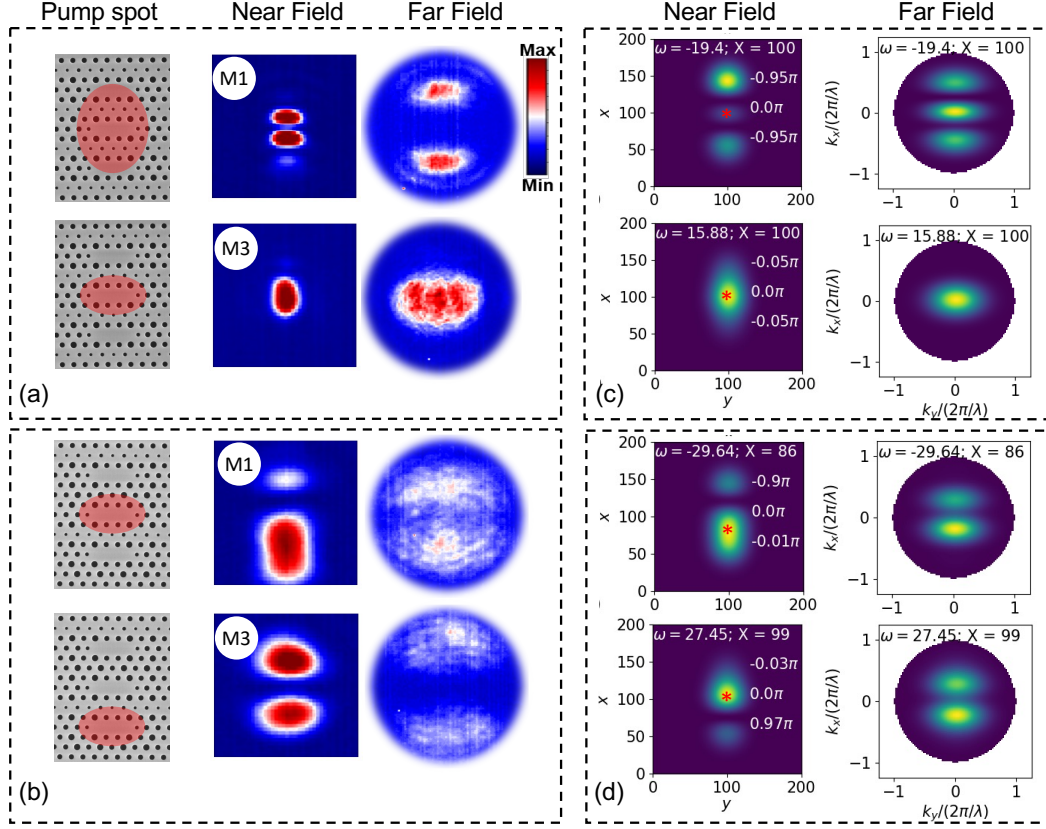


FIG. 7. Spatially resolved mode PL with non-uniform couplings: non-zero modes. (a),(b) Experimental results. (c),(d) Numerical simulations (CMT), $N_{max} = 0.27$, with point excitations X marked as red asterisks in the near field patterns, and also at the crosses with labels M1-M3 in Fig. 3(c). (a) and (c): $h_{12} = -0.1$, leading to the same coupling sign and $|K_{12}| < |K_{23}|$; (b) and (d): $h_{12} = -0.35$, leading to flipped coupling sign and $|K_{12}| > |K_{23}|$. Experimental near-field patterns are obtained imaging the sample plane on an InGaAs camera, while far-field patterns are obtained imaging the back focal plane of the microscope objective. CMT near-field patterns are obtained as the coherent superposition of cavity fields, $I^{(j)}(x, y) = |E^{(j)}(x, y)|^2$, where $E^{(j)}(x, y) = \sum_n \exp\{-[(x - x_n)^2 + y^2]/\sigma_c^2\} A_n^{(j)}$, with $\sigma_c = 30$ and $A_n^{(j)}$ the cavity amplitudes of mode j . CMT far-fields are obtained Fourier transforming $E^{(j)}(x, y)$.